

# Controllable Surface Haptics via Particle Jamming and Pneumatics

Andrew A. Stanley, *Student Member, IEEE*, and Allison M. Okamura, *Fellow, IEEE*

**Abstract**—The combination of particle jamming and pneumatics allows the simultaneous control of shape and mechanical properties in a tactile display. A hollow silicone membrane is molded into an array of thin cells, each filled with coffee grounds such that adjusting the vacuum level in any individual cell rapidly switches it between flexible and rigid states. The array clamps over a pressure-regulated air chamber with internal mechanisms designed to pin the nodes between cells at any given height. Various sequences of cell vacuuming, node pinning, and chamber pressurization allow the surface to balloon into a variety of shapes. Experiments were performed to expand existing physical models of jamming at the inter-particle level to define the rheological characteristics of jammed systems from a macroscopic perspective, relevant to force-displacement interactions that would be experienced by human users. Force-displacement data show that a jammed cell in compression fits a Maxwell model and a cell deflected in the center while supported only at the edges fits a Zener model, each with stiffness and damping parameters that increase at higher levels of applied vacuum. This provides framework to tune and control the mechanical properties of a jamming haptic interface.

**Index Terms**—Haptic device design, haptic I/O, particle jamming, tactile display.

## 1 INTRODUCTION

HIGH-QUALITY haptic feedback requires not only accurate kinesthetic feedback but also realistic cutaneous feedback of finger pad contact area, textures, and high-frequency vibrations. Encountered-type tactile displays aim to recreate realistic haptic sensations by producing physical environments for a user to explore directly with his or her hands. Unlike sight and hearing, touch is bidirectional in that the haptic sensations delivered by an environment depend not only on its physical state but also on the manner of the user's exploration or manipulation. A tactile display that accurately mimics the shape of an environment does not suffice to realistically recreate the feel of that environment; it must also deform and comply accordingly to the user's applied forces and motions. This article presents a novel tactile display that is capable of independent control of both its geometry and its mechanical properties simultaneously using pneumatics and a technique known as particle jamming, in which a flexible membrane filled with a granular material changes rigidity with the application of a vacuum.

One potential application of our tactile display concept arises in medical simulation. Haptic feedback serves as an important element of a clinician's diagnoses and decision regarding many procedures.

- A. A. Stanley and A. M. Okamura are with the Department of Mechanical Engineering, Stanford University, 424 Panama Mall, Bldg 560, Stanford, CA 94305.  
E-mail: [astan@stanford.edu](mailto:astan@stanford.edu); [aokamura@stanford.edu](mailto:aokamura@stanford.edu)

This work was supported by U.S. Army Medical Research and Materiel Command (USAMRMC; W81XWH-11-C-0050) and by a National Science Foundation Graduate Research Fellowship.

Palpation is often necessary to identify subcutaneous anatomical landmarks or to differentiate between similarly shaped objects [1]. By including a tactile display, virtual reality-based simulation can help clinicians gain experience tuning their sense of touch prior to performing a procedure on an actual patient. A tactile display with both controllable geometry and mechanical properties increases the variety of scenarios that a single display can accurately represent. With sufficient modeling of the underlying jamming phenomenon, the mechanical parameters of the display can be tuned to better match existing rheological models of biological tissues [2] to further increase realism and broaden the display capabilities.

Our previous research on this topic resulted in the Haptic Jamming [3] interface, including the implementation of a four-cell array of particle jamming cells with basic measurements of its shape and stiffness output capabilities and a human perception study of these outputs on a single-cell display [4]. In this work, we develop two key new contributions: improving the shape output controllability and modeling the variable mechanical properties. We describe a twelve-cell version of the array with novel design features: vacuum lines embedded into the silicone and a solenoid-actuated reel for pinning nodes between cells to reduce the device height profile and enhance the resolution of the geometry output capabilities. Furthermore, in comparison to the data collected in [3], in this paper we conduct more comprehensive force-displacement tests that allow us to develop rheological models of the particle jamming cells that more completely describe the forces a user feels during interaction. These models also provide a basis for tuning the

display to match existing models by adjusting the vacuum level.

## 2 BACKGROUND

The modeling, implementation, and underlying paradigm of our tactile display all build upon prior work in their respective fields. The subsections below describe particularly relevant work in existing encountered-type haptic displays, applications of particle jamming, and modeling of jammed systems.

### 2.1 Encountered-Type Haptics and Digital Clay

The Haptic Jamming interface can be considered an encountered-type haptic display because the user is free to explore the surface directly with his or her hands, rather than wearing or holding a device that constrains the exploration movements in any way. Within encountered-type haptic displays, the concept of “Digital Clay” [5], which can change shape both under the control of the computer and the user, represents an ideal for an advanced form of 3D computer input and output user interface. One possible implementation of “Digital Clay” consists of an array of fluid-driven actuators [6]. Additional display implementations include arrays of shape memory alloys [7], pneumatics [8] [9], and pins [10]. The continued development of soft robotics [11] has also led to some creative user interfaces [12].

Other approaches that adjust mechanical compliance properties instead of shape include tactile arrays of electrorheological fluids [13], which transform from liquid to plastic states with the application of an electric field, and magnetorheological fluids [14], which change stiffness via a magnetic field. Working towards achieving both adjustable geometry and compliance in a single display, recent work using an air jet allows simultaneous and independent control of the perception of both properties [15] [16].

### 2.2 Particle Jamming in Robotics and Haptics

The ability to rapidly switch a material between rigid and flexible states has inspired many applications, several within the field of robotics. A particle jamming end effector can provide a less expensive substitute for a robotic gripper, as demonstrated in [17], where the robot presses the mass of granular material in its unjammed state around an object before jamming it to gain a rigid hold. Expanding the particle jamming medium from the end effector to the whole manipulator provides a robust, low-cost alternative to standard solid mechanical robotic arms [18].

In a medical application, a long, thin particle jamming tube has been tested for bending stiffness with the future goal of applying the technology to an endoscope with controllable rigidity in Natural Orifice Translumenal Endoscopic Surgery [19]. This could

allow an endoscope to bend freely during insertion before switching to a rigid state. Jamming in combination with pneumatic pressure can also act as an alternative actuator and enable robotic locomotion [20].

Particle jamming has also produced several novel user interfaces for human-computer interaction. These include deformable surfaces on tabletops and the backs of screens [21] [22] and deformable mesh structures [23]. On a larger scale, Mitsuda *et al.* used a wearable display that spanned the length of the arm to simulate moving through stiff or viscous virtual environments by jamming Styrofoam beads in a long, soft vinyl tube [24].

### 2.3 Physical Models of Jamming

The scientific exploration of granular material and the jamming phenomenon spans decades of physics research. Cates *et al.* introduced the concept of force chains to explain the transition of a jammed system of granular material into an unjammed system in which the particles can flow under the application of stress [25]. The force applied to a given particle in a jammed system is transmitted directly to the particles contacting it in the direction of force, resulting in force chains along the direction of compression. These force chains can be imaged with cross-polarized filters and verified by computer models using probability distributions of inter-particle forces [26] [27]. Since such a force chain can only support loading along its axis, any load along a different axis large enough to overcome the static friction between the surfaces of particles causes the particles, and therefore the force chains, to rearrange. Thus, [25] presents the argument that the jammed media are “fragile” and unable to support incremental loading without plastic deformation. The force that a homogeneously jammed body can support under this model can be predicted by summing over the individual force chains with the probability distribution for inter-particle forces.

Building upon this research, Lui and Nagel proposed that when the media includes materials beyond rigid particles the jamming concept can be expanded into much broader systems, from temperature transitions of glass to load transitions of foams [28] and the jammed state is no longer totally fragile. As further explained in [29], a body of softer particles acts elastic as a whole up to the point that the maximum ratio of shear stress to normal stress reaches the friction coefficient of the particles and they slide to rearrange, plastically deforming the body as a whole.

Delving even deeper into the jamming analysis of granular systems, Bagi proposes a model using structural mechanics methods that covers not only deformable particles, but also particles of arbitrary shape, with rotational as well as translational degrees of freedom, and that are capable of transmitting tangential contact forces as well as normal forces [30].

This model examines each particle individually to include every external load, contact force, support reaction, particle displacement, contact deformation, surface curvature, and boundary deformation of the entire system, and the work even includes numerical examples for systems of three and four granules.

However, characterizing such detail (down to the level of individual particles) remains infeasible for most real systems, and many applications would benefit from more macroscopic models. Some previous work does include experiments to measure specific bulk properties of various particle jamming materials, such as the strength-to-weight ratio and absolute strength [18] as well as the particle hardness and bending stiffness [19]. In this work, we develop rheological models that more generally describe the force-displacement characteristics of jamming haptic displays and the effects of vacuum level. While we sought to derive as much of our modeling as possible directly from the principles described in the physics literature, we follow a more phenomenological approach, explaining our data in a manner consistent with the fundamental theory when not derived directly from the theory. As a result, some characteristics of these models are specific to the experimental setup and may vary for other jamming materials and configurations.

### 3 MULTI-CELL DEVICE FOR VARIABLE SURFACE GEOMETRIES

The novelty of Haptic Jamming lies largely in its ability to adjust both its mechanical and shape properties simultaneously. In [3] we presented a four-cell prototype consisting of an array of hollow hexagonal silicone cells with a circumscribing diameter of 1.25 inches (32 mm) filled with coffee grounds. A vacuum line with a valve to each cell can make any individual cell rigid by jamming the particles inside. By selectively jamming individual cells before increasing the pressure in the chamber below the array, only the soft cells will deform outward while the rigid cells will remain flat. In addition, leaving a set of neighboring cells soft while pressurizing the underlying chamber allows them to combine to form larger lumps. However, since the thin layer of silicone around the edge of each cell does not become rigid it can act like a hinge joint that allows even the rigid cells to rotate about their edges with the increased pressure.

In our earlier prototype we used two air cylinders aligned below each of the two nodes of the four-cell hexagonal array to selectively pin or unpin each node from its starting height to prevent the rigid cells from rotating. We define a node as any place where more than two cells meet that is not along the outer edge of the surface. Thus, through various combinations of node pinning, cell jamming, and chamber pressure adjustment operations the surface can rapidly (~1

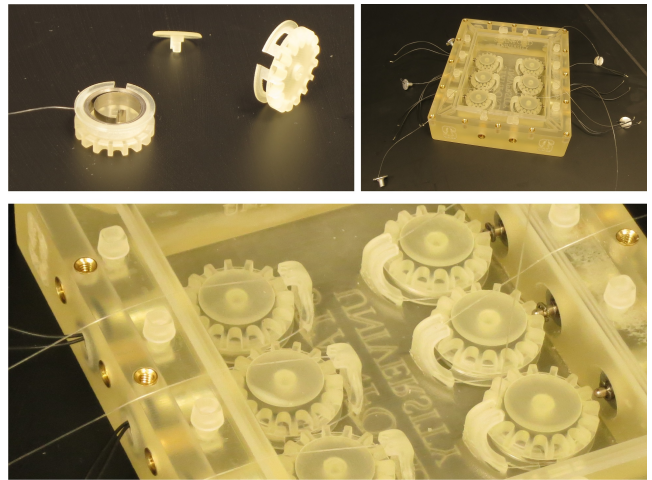


Fig. 1. Photos of two reels, one with a torsional spring, and a cap (top left), the full box with all solenoids and reels assembled (top right), and a close up showing the inner workings of the box (bottom).

second) reconfigure between a variety of contours and stiffnesses. Here, we have constructed a twelve-cell array of one-inch square cells (25.4 mm per side) with significant design changes to reduce form-factor and improve performance as a controllable surface display. Much of the setup matches that described in [3], including the pressure regulator (QB3TFEE003-S17, Proportion Air, McCordsville, Indiana) with a 0.5 second rise time for step pressure changes for the chamber and three-way solenoid valves (V1A04-BW1, Mead Fluid Dynamics, Inc., Chicago, IL) to vacuum or exhaust each of the cells. A custom graphical user interface controls a DAQ (USB-6343 X Series, National Instruments, Austin, TX), which sets the analog voltage to the regulator and the digital voltages to the bases of NPN bipolar junction transistors (2N3904, Fairchild Semiconductor, San Jose, CA) to open and close the valves electronically.

#### 3.1 Solenoid-Actuated Reels to Pin Nodes

The air cylinders used in the four-cell array provided a robust solution to pin the nodes without requiring any electromechanical actuators in the actual display, but a number of drawbacks led us to assess alternate designs. The air cylinders greatly increased the vertical profile of the device because, for any vertical travel of the surface of the display, at least as much space below the surface is required to fit the rod in its starting configuration. Second, pressurizing the top of the air cylinder pins the node at its lowest height regardless of the height of the node before the pressurization; it effectively acts a digital switch with no analog resolution.

To work around the height drawbacks of air cylinders and to reduce costs we designed a set of solenoid-actuated reel systems to pin the nodes, demonstrated

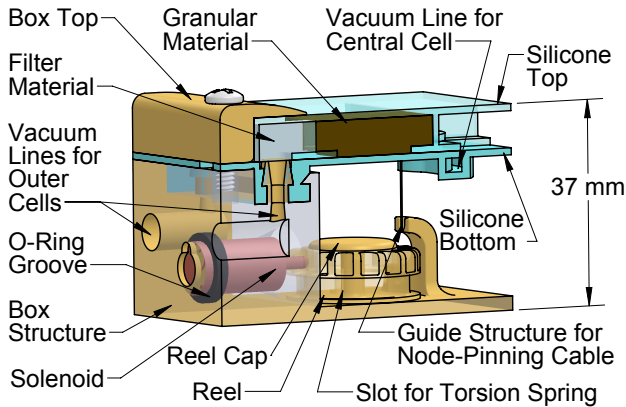


Fig. 2. A cross section of the display shows the inner workings of one of the six solenoid reel systems and some of the embedded vacuum lines.

in the accompanying video. Figure 1 includes a set of photos of the solenoid reel system and Figure 2 shows a cross sectional view of one part of the full device. We printed all custom parts on a Projet HD 3500 multi jet modeler (3D Systems, Rock Hill, SC). A 0.3 mm diameter nylon cable ties onto one side of a modified aluminum binding post that screws into the other side of the binding post that is embedded into the silicone on the bottom side of the node. This thin cable feeds through a support structure built into the box directly beneath the nodes and out the bottom of this structure tangent to the lower half of one of the reels. The cable wraps around the outside of this part of the reel, and on the inside a small torsional spring provides a small rotational tension that reels in the cable when the chamber is depressurized. The upper half of the reel consists of a set of 16 small teeth designed to fit the plunger of a pull-type miniature solenoid (SOTUL01001724C-S-63-38-42K, Magnetic Sensor Systems, Van Nuys, CA) between them. The reel and the inner end of the torsional spring slide over an axis built into the bottom of the air chamber with a small slip-fit cap that holds the reel in place.

When the solenoid is not activated, the plunger extends into the reel between two of the teeth, preventing it from spinning. This effectively pins the node at its previous height. Activating the solenoid pulls the plunger from the reel, allowing it to spin freely. If no chamber pressure is present, the torsional spring will reel the node back to its starting height, or if the chamber is pressurized the node will rise to its equilibrium height from the force on the underside of the silicone. The solenoid is embedded into the wall of the box with an o-ring to prevent air leakage through the holes for the electrical leads, and is controlled by the same transistors as the solenoid valves.

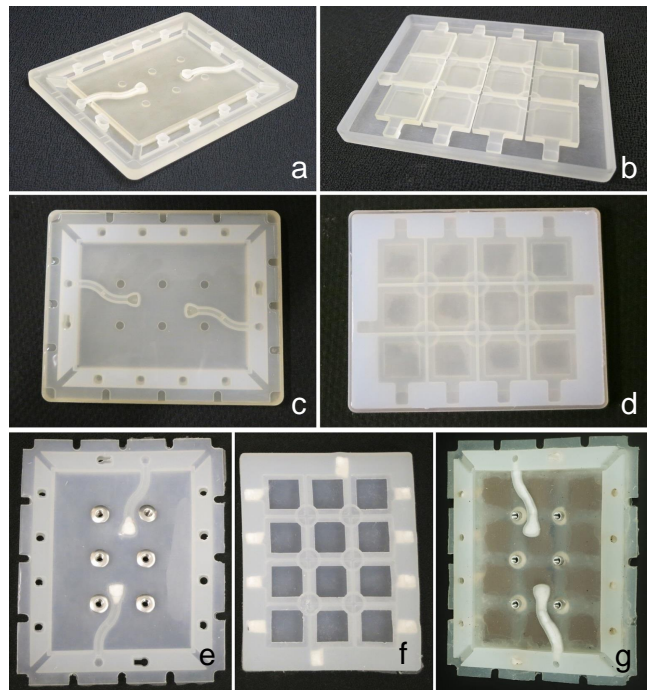


Fig. 3. Various stages of the silicone molding process: Empty molds for the bottom (a) and top (b) pieces of silicone, filled molds (c, d), and the pieces removed from the molds (e, f) with filter material and binding posts before gluing the two pieces together (g) and filling the cells.

### 3.2 Embedded Vacuum Lines

While the solenoid reel system greatly reduces the vertical profile of the node-pinning portion of the device, it also introduces some complexities that prevented reducing the overall vertical profile of the array. With the original prototype, tubes for the vacuum lines entered the main chamber via through-wall push-to-connect adapters with o-ring seals. The tubes then glued into a silicone nub that protruded from the center of the bottom of each cell. With the rigidity of the air cylinder rods, the tubes could bend around them to get to the through-wall connectors. With six fishing lines hanging from the bottom of the twelve-cell array, however, this would create a tangled mess, and the minimum bend radius of the tubing would present an issue for a shorter device. In addition, at the highest chamber pressures the tubes can start to poke through the surface of the display from below.

Designing around these constraints, we developed a method to embed the vacuum lines into the bottom layer of the silicone. The cross-sectional view of the box in Figure 2 helps explain the basic concepts behind our design. As with previous designs, the silicone consisted of two separate pieces that we glued together with Sil-Poxy silicone adhesive (Smooth-On, Inc.) after the molding process. The top piece of silicone extends 12.7 mm beyond the outer edges of

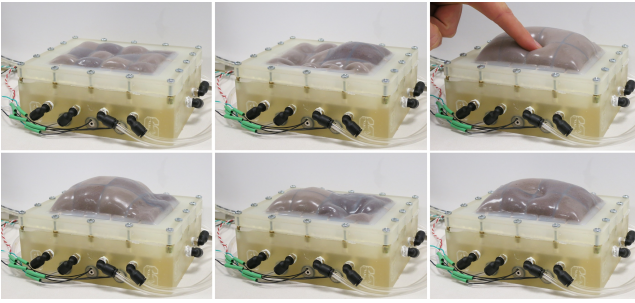


Fig. 4. A small subset of the configurations the controllable surface haptics display can present, including a checkerboard pattern of stiffness regions (top left) and a lump consisting of nine neighboring cells (bottom left). If a soft surface is vacuumed while the user is interacting with it (top right) it will hold that shape rigidly (bottom right). The accompanying video shows real-time configuration changes under computer control.

the particle jamming cells with small spaces connected to the side of each cell on the outer edge of the array. We filled these small spaces with a polyester felt filter material to prevent the vacuum from pulling the coffee out of the cell. These spaces line up with vertical channels in the bottom piece of silicone that snap over hollow cylinder- and cone-shaped protrusions in an elevated channel that runs along the inner edge of the box. To bottom piece of silicone also snaps into this elevated channel to prevent air in the pressurized chamber from leaking into the vacuum channels. Threaded brass inserts press-fit into holes in the side of the box that connect to the box protrusions that feed the vacuum to the cells.

Vacuuming the inner cells of the array without tubing presents an additional challenge because these cells cannot connect directly to the outer edge of the top piece of silicone. To work around this, we designed channels into the mold of the bottom piece of silicone that connect the center of the inner cells to the outer edge of the silicone from underneath. Creating this channel requires more complicated molds with multiple 3-D printed pieces that slip-fit together, shown in Figure 3 along with the resulting pieces of silicone. To prevent the silicone channel from collapsing in upon itself when vacuumed, we fill it with polyester felt filter material.

### 3.3 Variable Geometry Output Capabilities

In addition to providing separately controllable stiffness in twelve regions across a surface, the multi-cell array greatly increases the number of and types of geometries the controllable surface haptics display can present. The cells can essentially act like pixels in a tactile image; the greater the number of pixels in the image, the more complex geometries the device can display. Vacuuming any set of cells and pinning or unpinning any nodes can all occur simultaneously

and require less than a tenth of a second, so the duration of any control sequence is essentially set by the amount of time it takes for the pressure regulator to inflate the chamber. For example, the control sequence of vacuuming all but four neighboring cells in a  $2 \times 2$  square, unpinning the node in the middle of those four cells, increasing the chamber pressure to balloon those four cells upward, vacuuming those cells and un-vacuuming the others will create a rigid four-cell lump in one region of the display surrounded by soft cells. This configuration and others are shown in Figure 4.

The custom graphical user interface to control the device includes buttons to automatically create single-cell,  $2 \times 2$ , and  $3 \times 3$  lumps in any region of the display in either a soft or rigid configuration. Given the capabilities of the solenoid reel system to pin a node to prevent it from rising above any given height, longer control sequences involving multiple levels of inflation could create even more interesting geometries beyond single lumps. With six separate pressure adjustments at ascending levels, each of the six nodes could be pinned at separate heights, and even more pressure adjustments would allow a variety of inflation levels for many cells by vacuuming them at different points in the sequence. The accompanying video shows some examples of the display reconfiguring in real time under computer control.

## 4 MECHANICAL MODELING OF PARTICLE JAMMING DISPLAYS

Even without the complexities of a pressurized chamber and node pinning mechanisms, particle jamming alone can create a compelling haptic interface [22]. In medical training, for example, a single sheet of jamming material with adjustable mechanical properties could be used to simulate different types of biological tissue covering other anatomical features in a palpation task. Despite the relatively low spacial resolution, clinician advisors suggest that even a single particle jamming cell could provide a valuable dynamic aspect to the simulation environment. In this section, we aim to develop a model that can predict the forces a user would feel while interacting with a particle jamming display in a given configuration, as well as provide controllable parameters that a designer can tune to create a system capable of exhibiting any of an achievable set of desired physical properties.

### 4.1 Methods and Setup

As the existing models of particle jamming [18][25][28][29][30] predominantly use compression tests as a baseline, we started with a set of compression tests to build our rheological models. Given our interest in human interaction forces, we designed our setup to closely match the



Fig. 5. The experimental setup used to collect force-displacement data.

configuration of a Haptic Jamming device as a user might feel it with his or her finger. We built a set of individual circular particle jamming cells consisting of a hollow cylindrical shell of silicone rubber (Ecolflex 00-30, Smooth-On, Inc., Easton, PA) filled with coffee grounds. A tube to the vacuum supply glues into the bottom of the cell and the entire cell clamps over an air pressure-regulated chamber. Removable acrylic pieces, each with a circular cutout of a different diameter, can be switched out from underneath the cells to change between configurations in which a cell is either rigidly supported from below by the acrylic or unsupported for the diameter of the cell. We describe the manufacturing of these individual cells and their setup in much greater detail in [3]. We collected data during the compression tests by attaching an force/torque sensor (Nano 17, ATI, Apex, NC) to the end effector of a Phantom Premium (Sensable Technologies, Inc., Wilmington, MA) with a 3-D printed 9.5 mm diameter hemispherical attachment affixed to the other side of the force sensor (Figure 5).

## 4.2 Supported Compression Model

### 4.2.1 Formulating Model Framework

For each of eleven vacuum levels ranging from 0-25 inHg, where 29.9 inHg is a complete vacuum, we recorded compression and rebound data for ten palpations per level with the cell supported from below. Figure 6 shows the raw data from one sample trial each for six of the vacuum levels. We chose inches of mercury (inHg) as the units for vacuum in place of the metric millibars because all of the instrumentation of our setup used inHg to measure vacuum.

A number of key features stand out immediately upon examination of these force-deflection curves. First, there is significant hysteresis present in each of the curves; the forces recorded during the compression are much greater than those recorded during the

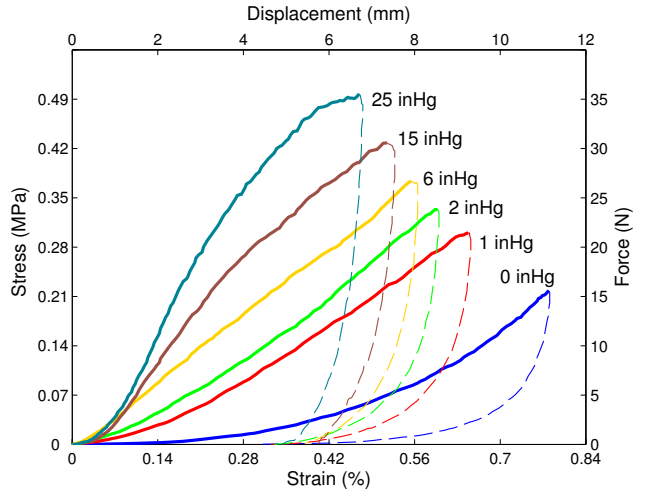


Fig. 6. Raw data from one sample of the ten compression trials from each of six of the eleven vacuum levels tested, with conversions to stress and strain. Rebounds are shown dotted.

rebound for any given displacement. This indicates that the system absorbs energy during each cycle. Thus the mechanical model must include damping or friction. Second, the data indicate permanent deformation of the cell from a compression test because the deflection never returns to zero, even when all force has been removed. This deformation is also visually evident from inspecting a cell after a compression test. In biological tissue modeling, the term stress relaxation describes a decrease in stress toward a steady-state value for a material in constant strain; when building a rheological model of springs and dashpots for such a system, stress relaxation requires a dashpot in series with a spring, known as the Maxwell viscoelastic model [2]. This model and our notation for the equations governing it are shown in Figure 7.

Additionally, while not immediately obvious from visual inspection of the force-deflection curves, the data indicate nonlinearity in the mechanical model; the stiffness shows dependence on the compression depth. Before external compression loads are applied, the force chains of particles in a jammed system act like sets of springs in series because each particle can deform elastically until the applied force overcomes the static friction between the particles in the least stable chains, as described in Section 2. At this point these particles slide against one another and rearrange to form shorter, more stable force chains. With fewer particles in each force chain, the effective stiffness of the system actually increases with increasing compression depth such that the elastic force of the granules,  $F_e$ , follows the relation

$$F_e = k_{gr} x_1^n, \quad (1)$$

where  $k_{gr}$  is the stiffness constant of the granular material,  $x_1$  is the elastic component of the compres-

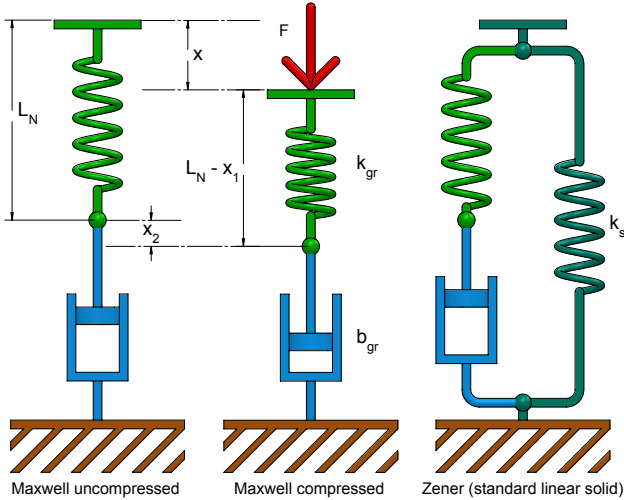


Fig. 7. We propose non-linear versions of the Maxwell and Zener models to fit the behaviors of jammed granules in compression and of an unsupported jammed cell, respectively.

sion depth, and  $n$  is greater than one. A brute-force-search optimization, using the modeling techniques described later in this section, fit a value of  $n = 1.998$ . For modeling simplicity and to account for noise in the data we rounded this to  $n = 2$ , such that effective stiffness increases linearly with compression depth.

From a microscopic perspective, a jammed system under compression shifts back and forth between elastic compression and plastic rearrangement of sliding particles with each shortening force chain. However, from a macroscopic perspective, various unstable force chains are rearranging constantly as the deflection increases with the applied load while more stable chains maintain the load, resulting in a relatively continuous friction force from the rearranging chains combined with a relatively continuous elastic deformation force from the more stable chains. If the particles were infinitesimally small, a truly continuous force would result from the compression, but for coarser granules like the coffee grounds used in our experiments the small discontinuities are not always obscured by the scale of the larger effects. These create low-magnitude, high-frequency accelerations that, while essentially inseparable from sensor noise in data, could manifest in human perception. Users of our haptic displays who palpate to significant depths often comment on the salience of the underlying sensation of the granules shifting against one another.

The individual friction forces between particles are traditionally modeled by a constant-force Coulomb friction rather than linear damping. However, the friction force in the system as a whole does increase with increasing compression velocity because a larger number of particles are forced to rearrange at any given time. Thus, from a macroscopic perspective, a

linear damping model provides a better fit for the sum of the friction forces. For our modified Maxwell model of a non-linear spring in series with a dashpot, the external force applied is equal to both the force in the spring and the force in the damper such that

$$F = k_{gr}x_1^2 = b_{gr}\dot{x}_2, \quad (2)$$

where  $x_1$  refers to the displacement of the spring below its natural length and  $x_2$  refers to the displacement of the dashpot below its starting length and

$$x = x_1 + x_2, \quad (3)$$

such that the total displacement of the system is the sum of the displacement of each component in series. Figure 7 illustrates this system and its notations.

#### 4.2.2 Parameter Fitting and Results

To fit the parameters  $k_{gr}$  and  $b_{gr}$  to a given set of compression data requires some manipulation because the total force and total deflection data do not explicitly describe  $x_1$  and  $x_2$  without knowing the model parameters first. Given the initial conditions of starting with zero force and zero displacement, we can manipulate Equations 2 and 3 into the form

$$x = \sqrt{\frac{F}{k_{gr}}} + \frac{1}{b_{gr}} \int F dt, \quad (4)$$

so that  $x$  is now an independent function of  $F$  and the modeling parameters. Since  $x$  and  $F$  are both time-histories, we can represent Equation 4 in matrix form as an over-constrained system

$$\underbrace{\begin{bmatrix} x(0) \\ x(1) \\ \vdots \\ x(n) \end{bmatrix}}_X = \underbrace{\begin{bmatrix} \sqrt{F(0)} & \int F dt(0) \\ \sqrt{F(1)} & \int F dt(1) \\ \vdots & \vdots \\ \sqrt{F(n)} & \int F dt(n) \end{bmatrix}}_F \underbrace{\begin{bmatrix} \sqrt{1/k_{gr}} \\ 1/b_{gr} \end{bmatrix}}_C \quad (5)$$

and  $(F^T F)^{-1} F^T X$  provides the least squares solution for  $C$ . Rearranging the two components of  $C$  provides the least squares fits for the modeling parameters  $k_{gr}$  and  $b_{gr}$  for an individual compression test.

We calculated the fits of these parameters for each of the ten trials at each of the eleven vacuum levels, increasing the spacing between vacuum levels at higher values because the variance between trials increased noticeably with increasing vacuum. Box plots of these parameters are shown in Figure 8 with a weighted linear fit. The inverse of the variance at each vacuum level was used to weight the least squares fit [31]. As we would expect, the stiffness and damping coefficients increase with higher vacuum levels as the system becomes more jammed.

To quantitatively assess our model, we can evaluate Equation 4 with the force time-history data and the fit parameters for each compression trial and compare

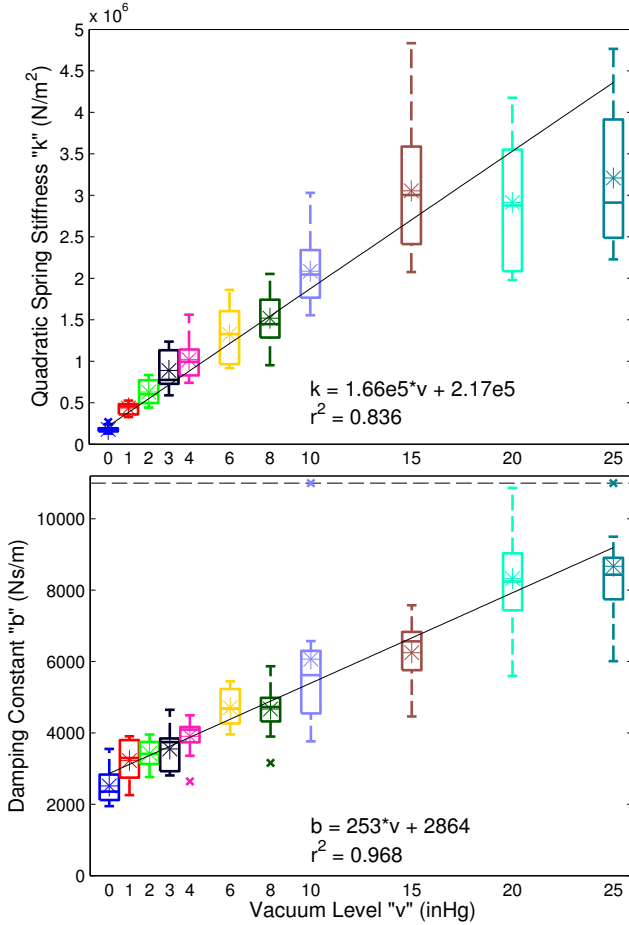


Fig. 8. Box plots of the fit parameters for supported cells. Each box includes the ten trials at that vacuum level, where the box edges mark the 25th-75th percentile with a line through the median, whiskers mark all data not considered outliers, and x's denote outliers. A star marks the mean and extreme outliers are clipped to the black dotted line. A linear regression with inverse-variance weighting is also shown.

these modeled displacements with the actual displacement time-histories. Furthermore, for an even more comprehensive evaluation of the model to demonstrate that its inverse also holds, we can manipulate Equation 4 into the form

$$\dot{F} = 2\left(\dot{x} - \frac{F}{b_{gr}}\right)\sqrt{k_{gr} * F}. \quad (6)$$

This allows use of the displacement time-history data and the fit parameters to numerically integrate for a modeled time-history of the resulting force. Figure 9 shows the results of both the force and displacement models for each of the sample trials shown in Figure 6. These plots suggest that the model fits fairly well when any vacuum, regardless of how small, is applied to the system to jam it, but that the model is not as accurate for the unjammed system when no vacuum is applied.

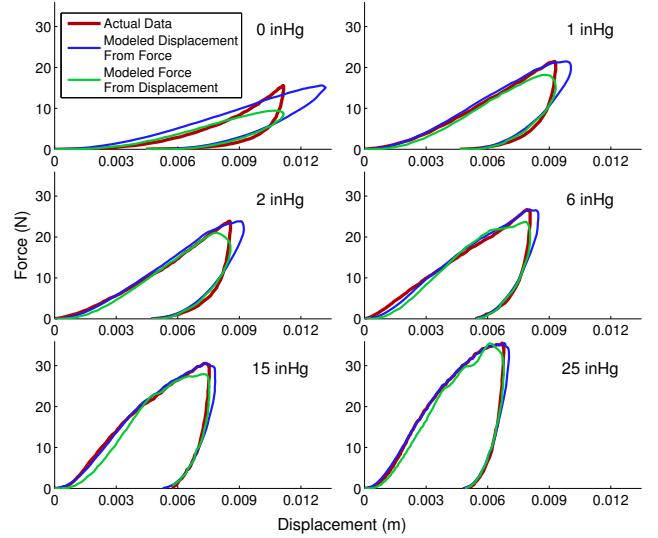


Fig. 9. Curve comparisons provide a qualitative evaluation of the model results for the trials in Fig. 6 which includes six different vacuum levels in the range of 0-25 inHg.

To quantitatively support this suggestion, we calculate two error metrics each for both the displacement modeled from the force,  $x_{model}$ , and the force modeled from the displacement,  $F_{model}$ . For each compression trial,  $e_{avg}$  denotes the average error across all time-steps and  $e_{prop}$  denotes the error at each time-step as a proportion of the actual value at that time-step, averaged across all time-steps. Time-steps with actual forces and displacements of less than 0.5 N or 0.0001 m, respectively, were removed from the proportional error calculations to avoid exceedingly large errors from the division by very small values in the first and last few time-steps.

The mean  $e_{avg}$  across all trials at all vacuum levels was calculated as  $2.87 \times 10^{-4}$  m for the  $x_{model}$  data and 1.41 N for the  $F_{model}$  data. The mean error metrics at each individual vacuum level are shown in Figure 10. Removing the  $1.21 \times 10^{-3}$  m  $e_{avg}$  and 2.00 N  $e_{avg}$  at zero vacuum leaves  $1.95 \times 10^{-4}$  m  $e_{avg}$  and 1.36 N  $e_{avg}$  for all  $x_{model}$  and  $F_{model}$  data, respectively, when any vacuum was applied to jam the system. Similarly, the mean  $e_{prop}$  across all trials at all vacuum levels was calculated as 5.38% for the  $x_{model}$  data and 19.05% for the  $F_{model}$  data. Removing the 15.36%  $e_{prop}$  and 33.03%  $e_{prop}$  at zero vacuum leaves 4.38%  $e_{prop}$  and 17.65%  $e_{prop}$  for all  $x_{model}$  and  $F_{model}$  data, respectively, when any vacuum was applied to jam the system. The  $e_{prop}$  errors are significantly higher for the  $F_{model}$  data than for the  $x_{model}$  because the cost function we used to fit the model parameters minimized error in  $x_{model}$ . The time-dependent nature of Equation 6 prevents us from fitting parameters that minimize error in  $F_{model}$ . The mean strain rates of trials ranged from 0.003 to 0.022 m/s, with local minimum and

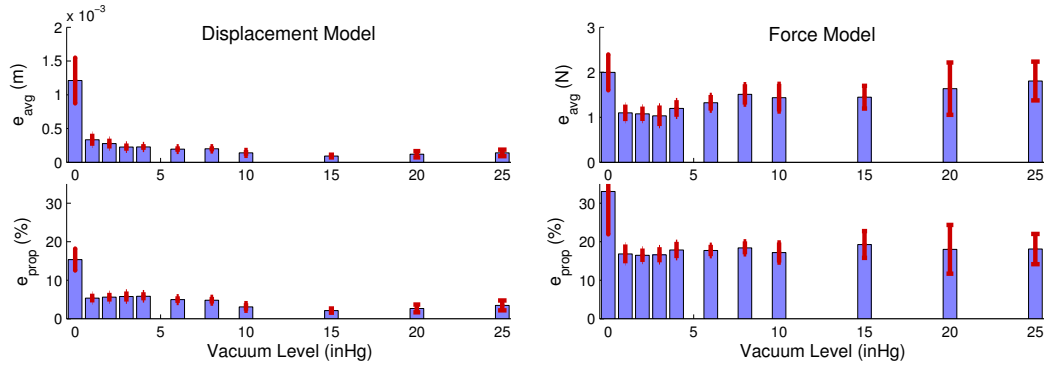


Fig. 10. Mean  $e_{avg}$  (the average error across all time-steps in a trial) and  $e_{prop}$  (the error at each time-step as a proportion of the actual value at that time-step, averaged across all time-steps) at each vacuum level tested for the displacement modeled from the force data and vice versa for the supported cell compressions. Error bars indicate one standard deviation from the mean.

maximum strain rates within trials, after smoothing to account for noise from differentiation, ranging from 0.001 to 0.038 m/s. While more complex models might better describe the data, the relatively simple lumped parameter model chosen here fits sufficiently well, even without a controlled strain rate, that we did not consider adding more parameters or using quasilinear viscoelastic models.

### 4.3 Unsupported Cell Model

While less relevant to the physics literature and previous models of jamming than the supported cell models, unsupported cell models provide more pertinent insight into the forces a user will experience while exploring a multi-cell array. In order for the array to functionally shift between various shape outputs pneumatically, the array must be suspended over a pressurized air chamber held by the silicone, similar to the set up for the unsupported cells in these tests. We performed two sets of palpations on three unsupported circular cells with diameters of 1, 1.5, and 2 inches (25.4, 38.1 and 50.8 mm). For each cell diameter in each set we conducted five trials at each of the same eleven levels of vacuum that we used in the supported compression tests. In the first of the two sets we controlled palpation location and direction but not the palpation depth. The raw data for the 1-inch diameter cell is shown in Figure 11. As with the supported compression tests, the data show that the cell becomes more rigid with increasing vacuum level as the particles jam.

Another noticeable characteristic of these data is that at high vacuum levels, in trials in which we palpated to sufficient depth, the compression portion of each curve seems to include distinct segments. Visual inspection of the cell during these palpations helps elucidate the physical phenomena behind each of these separate segments, as we illustrate in Figure 12. The cell starts as a thin cylindrical disk, supported

only by the silicone at its edges being clamped between two layers of acrylic. A cross-sectional slice of the cell closely matches the model of a beam supported by pin joints at the ends with a downward load applied at the center. Hooke's law tells us that for a beam bending in this configuration the deflection  $x$  at the center relates to the force  $F$  applied by the following equation

$$F = \frac{4ab^3 E}{d^3} x, \quad (7)$$

where  $d$  is the length of the beam,  $a$  and  $b$  are cross sectional dimensions, and  $E$  is the Young's modulus of the material, so the system looks like a linear spring where the coefficients of  $x$  are the effective stiffness. However, this relation only applies for elastic deformation and the jammed granular material also exhibits plastic deformation as the particles slide against each other in the cell. Unlike the normal deformation of the supported cell, the deformation of an unsupported cell occurs primarily in shear, so instead of force chains rearranging to increase the stiffness with depth, the effective stiffness from the bending cell remains constant until yield, modeled by a linear spring.

Before yielding, the cell's granules rearrange within it for some plastic deformation but the overall integrity of the disk shape is maintained, as shown in Figure 12c. Once the cell reaches its yield stress, the force-deflection curve levels out significantly and the disk collapses, as shown in Figure 12d. After this point, any further increases in force come from the stretching of the layers of silicone on the top and bottom of the cell, which explains why the slopes at the ends of the curves are all the same regardless of vacuum level. We model the silicone as a set of springs connecting the edges of the cell to the center. As the center point moves down with the displacement  $x$ , the angle of the orientation of the springs relative to

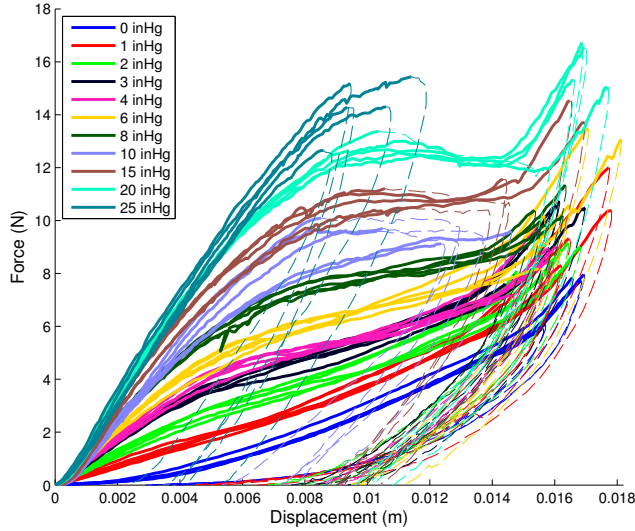


Fig. 11. Raw data from from the first set of palpations to varying depths in which the cell was not supported from below.

the horizontal,  $\theta$  is defined as

$$\theta = \arctan \frac{x}{r}. \quad (8)$$

Thus, the springs stretch a distance  $\delta$  defined by

$$\delta = \frac{x}{\sin \theta} - r, \quad (9)$$

where  $r$  is the radius of the cell. In addition to the silicone stretching a greater distance relative to the displacement for smaller cells, the silicone also has a larger effective stiffness,  $k_{si}$ , in these cells, proportional to the inverse of  $r$ , because the spring is shorter. To verify these relationships we performed sets of ten palpations on an empty cell of each size, and using a stiffness of  $10/r$  N/m the data fit the equations with an average  $r^2$  value of 0.946.

Including the effects of the silicone adds a non-linear spring in parallel with the spring and dashpot series of the jammed granular material. The overall resulting configuration of a spring in parallel with a spring and dashpot in series is known as a Zener model, except that the effective spring of the silicone is non-linear and the cell yields at high levels of vacuum and deflection. We can subtract the forces of the silicone from the total measured forces to fit parameters to the spring and dashpot of the jammed material, but to use the least squares methods described in Equations 4 and 5 we also needed to collect a second set of data in which the palpations were controlled to stop at a depth of 7.5 mm, before any of the cells had reached total yield. The raw data from this second set and their fit parameters are shown in Figure 13.

We used the same metrics to evaluate the unsupported cell model as we used for the supported cell compression tests. The mean  $e_{avg}$  across all trials at all vacuum levels and cell diameters was calculated

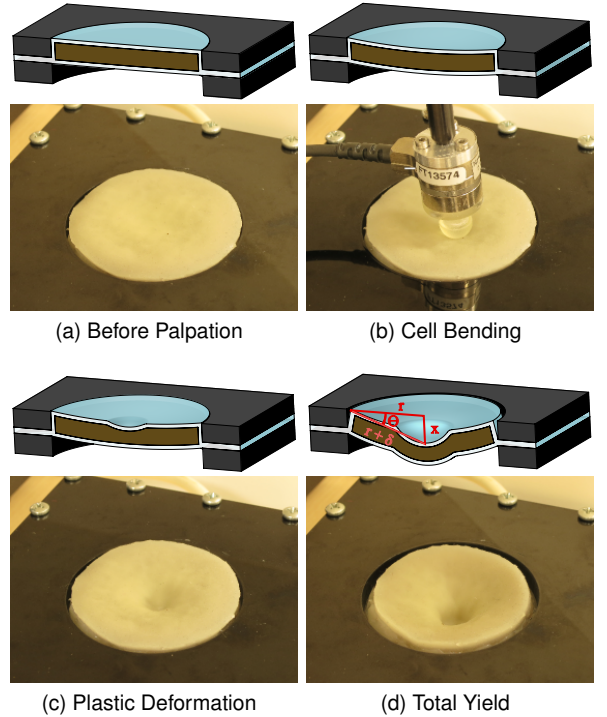


Fig. 12. For deep palpations without support beneath the cell, the cell undergoes multiple stages of deformation that manifest themselves in the force-deflection curves.

as  $1.78 \times 10^{-4}$ m for the  $x_{model}$  data and 0.146N for the  $F_{model}$  data. The mean  $e_{prop}$  across all trials at all vacuum levels was calculated as 3.62% for the  $x_{model}$  data and 5.56% for the  $F_{model}$  data. The mean error metrics at each individual vacuum level for each of the three cells are shown in Figure 14. Overall these models fit the data slightly better than the supported compression models, and the data also did not show as large of a deviation for zero vacuum in the unsupported cell models.

As shown in Figure 13, the stiffness and damping coefficients of the model parameters depend not only on the vacuum level applied but also the diameter of the cell. Thus, an array capable of combining different numbers of cells into regions and lumps of varying sizes both improves the geometric display variability and also broadens the spectrum of achievable mechanical properties.

## 5 CONCLUSION

While many tactile displays exist to adjust either the physical geometry that a user touches or the level of rigidity that the user feels, most conventional actuators prevent combining these two features into a single display. The implementation of the jamming display described in Section 3 greatly improves the shape output capabilities over earlier prototypes while also resolving many design issues

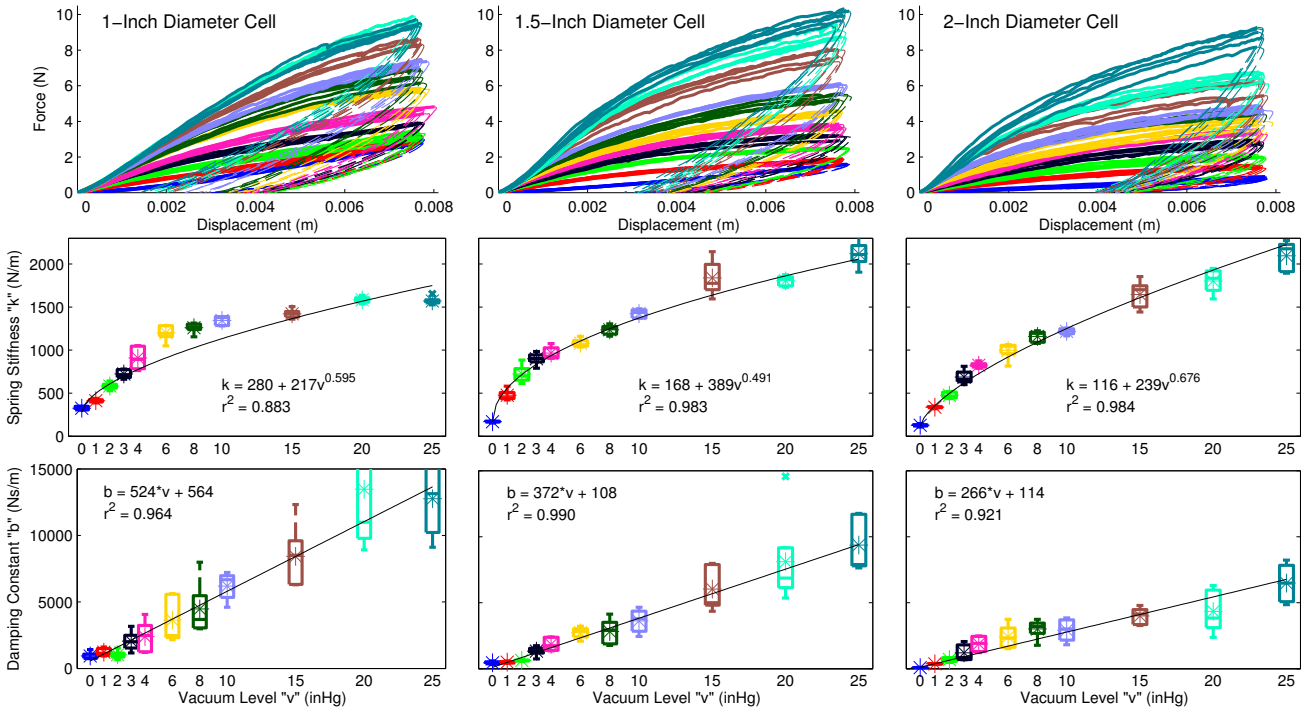


Fig. 13. Raw data from palpations with controlled depth in which the cell was not supported from below, and parameter fits to the spring and dashpot in series portion of the Zener model.

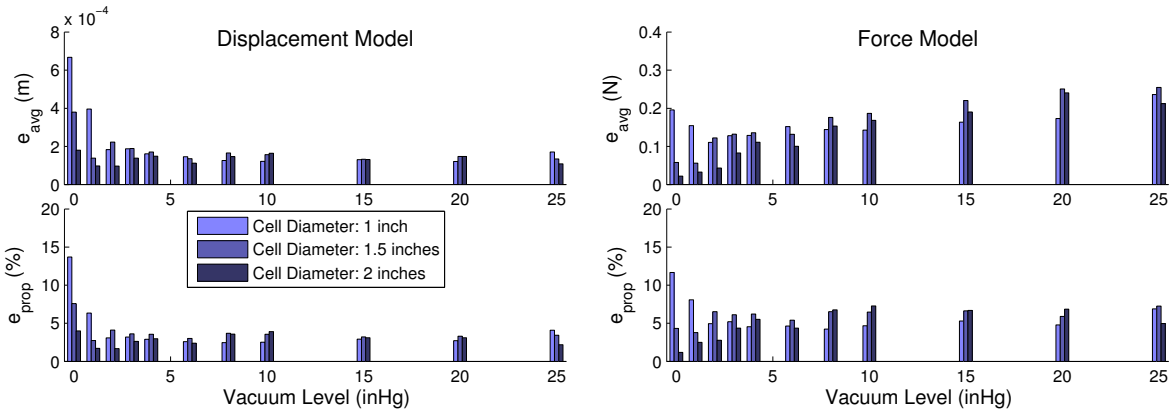


Fig. 14. Mean  $e_{avg}$  and  $e_{prop}$  at each vacuum level and cell diameter tested for the displacement modeled from the force data and vice versa for the unsupported cell palpations.

that inhibited their performance and prevented down-scaling in size. Future iterations will continue the effort to increase resolution and performance of the display while reducing cost and size. Furthermore, introducing sensors into the system could allow the device to simultaneously function as a user input and output for human-computer interaction, rather than exclusively as an output as it operates in its current form.

Representing a virtual environment accurately requires a precise physical characterization of the display so that the computer controlling the display can accurately render the environment in the physical world. Toward this end, this article developed rhe-

ological models to physically describe particle jamming systems in different configurations from a more macroscopic view than the models typically found in the physics literature for granular materials. Future studies evaluating the effect of material type, material thickness, and multiple contact points or interaction along the continuous surface on the parameters in these rheological models would prove useful for providing a broader database of all possible systems that could be simulated. Given such a database, a designer aiming to simulate a specific environment could first build a device from the materials and thicknesses best fit to cover the spectrum of stiffnesses and damping characteristics of the environment and then adjust

the vacuum level in real time to further tune the parameters in different parts of the environment. For example, many soft tissues are modeled by Zener or Maxwell models [2], so jamming displays could provide a useful tool in medical simulation to present various types of tissue interactions.

With the increase in shape output capabilities, a dynamic model of the surface deformation would greatly improve the computer-controllability of the geometry. Such a model will need to include variation of air pressure level, vacuum level in each individual cell, the heights of each node, and the sequence of operations as parameters to fully predict the shape output of the device. Ideally this model would also be invertible such that, given a desired three-dimensional surface geometry, the computer could calculate the sequence of vacuuming cells, pinning nodes, and increasing chamber pressure necessary to most closely match that desired configuration, and might involve FEM methods previously used for control of soft robots [32]. Ultimately, we will integrate the controllable surface haptics device into a more immersive virtual reality. We have explored mounting the device onto the end effector of a robot with hand tracking to create an encountered-type display [33] and plan to experiment with head-mounted displays and novel position sensors. This increases the workspace of a virtual environment, allowing a user to feel different shapes and material properties as they move around and explore different areas.

## ACKNOWLEDGMENTS

The authors thank Jim Gwilliam for his work developing the haptic jamming display concept and its original prototypes, Mark Stauber for his original design and prototyping of a previous version of the solenoid reel system, and Intelligent Automation, Inc. for their collaboration on using the particle jamming concepts for medical simulation.

## REFERENCES

- [1] S. Ullrich and T. Kuhlen, "Haptic palpation for medical simulation in virtual environments." *IEEE Transactions on Visualization and Computer Graphics*, vol. 18, no. 4, pp. 617–25, 2012.
- [2] S. Misra, K. Ramesh, and A. Okamura, "Modeling of tool-tissue interactions for computer-based surgical simulation: a literature review," *Presence: Teleoperators and Virtual Environments*, vol. 17, no. 5, pp. 463–491, 2008.
- [3] A. A. Stanley, J. C. Gwilliam, and A. M. Okamura, "Haptic jamming: A deformable geometry, variable stiffness tactile display using pneumatics and particle jamming," in *IEEE World Haptics Conference*, 2013, pp. 25–30.
- [4] A. M. Genecov, A. A. Stanley, and A. M. Okamura, "Perception of a Haptic Jamming Display : Just Noticeable Differences in Stiffness and Geometry," in *IEEE Haptics Symposium*, 2014, pp. 333–338.
- [5] J. Rossignac, M. Allen, W. Book, A. Glezer, I. Ebert-Uphoff, C. Shaw, D. Rosen, S. Askins, P. Bosscher, J. Gargus, I. Llamas, and A. Nguyen, "Finger sculpting with Digital Clay: 3D shape input and output through a computer-controlled real surface," in *Shape Modeling International*, 2003, pp. 229–231.
- [6] H. Zhu and W. J. Book, "Control Concepts For Digital Clay," in *IFAC Symposium on Robot Control*, 2003.
- [7] P. Taylor, A. Moser, and A. Creed, "A sixty-four element tactile display using shape memory alloy wires," *Displays*, vol. 18, pp. 163–168, 1998.
- [8] C.-H. King, M. O. Culjat, M. L. Franco, J. W. Bisley, E. Dutson, and W. S. Grundfest, "Optimization of a pneumatic balloon tactile display for robot-assisted surgery based on human perception." *IEEE Transactions on Biomedical Engineering*, vol. 55, no. 11, pp. 2593–600, 2008.
- [9] H. Iwata, H. Yano, and N. Ono, "Volflex," in *ACM SIGGRAPH 2005 Emerging technologies*, 2005, p. 31.
- [10] R. Howe, W. Peine, D. Kantarinis, and J. Son, "Remote palpation technology," *IEEE Engineering in Medicine and Biology Magazine*, vol. 14, no. 3, pp. 318–323, 1995.
- [11] D. Trivedi, C. D. Rahn, W. M. Kier, and I. D. Walker, "Soft robotics: Biological inspiration, state of the art, and future research," *Applied Bionics and Biomechanics*, vol. 5, no. 3, pp. 99–117, 2008.
- [12] L. Yao, R. Niiyama, J. Ou, S. Follmer, C. Della Silva, and H. Ishii, "Pneui: Pneumatically actuated soft composite materials for shape changing interfaces," in *ACM Symposium on User Interface Software and Technology*, 2013, pp. 13–22.
- [13] P. Taylor, "Advances in an electrorheological fluid based tactile array," *Displays*, vol. 18, pp. 135–141, 1998.
- [14] Y. Liu, R. Davidson, P. Taylor, J. Ngu, and J. Zarraga, "Single cell magnetorheological fluid based tactile display," *Displays*, vol. 26, no. 1, pp. 29–35, 2005.
- [15] J. C. Gwilliam, M. Bianchi, L. K. Su, and A. M. Okamura, "Characterization and Psychophysical Studies of an Air-Jet Lump Display," *IEEE Transactions on Haptics*, vol. 6, no. 2, pp. 156–166, 2013.
- [16] K. Inoue, F. Kato, and S. Lee, "Haptic device using flexible sheet and air jet for presenting virtual lumps under skin," in *IEEE International Conference on Intelligent Robots and Systems*, 2009, pp. 1749–1754.
- [17] J. R. Amend, E. Brown, N. Rodenberg, H. M. Jaeger, and H. Lipson, "A Positive Pressure Universal Gripper Based on the Jamming of Granular Material," *IEEE Transactions on Robotics*, vol. 28, no. 2, pp. 341–350, 2012.
- [18] N. G. Cheng, M. B. Lobovsky, S. J. Keating, A. M. Setapen, K. I. Gero, A. E. Hosoi, and K. D. Iagnemma, "Design and Analysis of a Robust, Low-cost, Highly Articulated Manipulator enabled by jamming of granular media," in *IEEE International Conference on Robotics and Automation*, 2012, pp. 4328–4333.
- [19] A. Loeve and O. van de Ven, "Vacuum packed particles as flexible endoscope guides with controllable rigidity," *Granular Matter*, vol. 12, pp. 543–554, 2010.
- [20] E. Steltz, A. Mozeika, N. Rodenberg, E. Brown, and H. Jaeger, "JSEL: Jamming Skin Enabled Locomotion," in *2009 IEEE/RSJ International Conference on Intelligent Robots and Systems*, 2009, pp. 5672–5677.
- [21] N. Aihara, T. Sato, and H. Koike, "Highly deformable interactive 3D surface display," in *ACM symposium on User Interface Software and Technology*, 2012, p. 91.
- [22] S. Follmer, D. Leithinger, A. Olwal, N. Cheng, and H. Ishii, "Jamming User Interfaces: Programmable Particle Stiffness and Sensing for Malleable and Shape-Changing Devices," in *ACM Symposium on User Interface Software and Technology*, 2012, pp. 519–528.
- [23] A. Mazzone, C. Spagno, and A. Kunz, "The HoverMesh: A Deformable Structure Based on Vacuum Cells," in *ACM SIGCHI International Conference on Advances in computer entertainment technology*, 2004, pp. 187–193.
- [24] T. Mitsuda, S. Kuge, M. Wakabayashi, and S. Kawamura, "Wearable Force Display Using a Particle Mechanical Constraint," *Presence: Teleoperators and Virtual Environments*, vol. 11, no. 6, pp. 569–577, 2002.
- [25] M. Cates, J. Wittmer, J.-P. Bouchaud, and P. Claudin, "Jamming, Force Chains, and Fragile Matter," *Physical Review Letters*, vol. 81, no. 9, pp. 1841–1844, 1998.
- [26] C. H. Liu, S. R. Nagel, D. A. Schecter, S. N. Coppersmith, S. Majumdar, O. Narayan, and T. A. Witten, "Force fluctuations in bead packs." *Science*, vol. 269, no. 5223, pp. 513–5, 1995.
- [27] T. S. Majumdar and R. P. Behringer, "Contact force measurements and stress-induced anisotropy in granular materials." *Nature*, vol. 435, no. 7045, pp. 1079–82, 2005.

- [28] A. J. and Liu and S. R. Nagel, "Jamming is not just cool any more," *Nature*, vol. 396, p. 21, 1998.
- [29] A. J. Liu and S. R. Nagel, *Jamming and Rheology: Constrained Dynamics on Microscopic and Macroscopic Scales*. CRC Press, 2001.
- [30] K. Bagi, "On the Concept of Jammed Configurations from a Structural Mechanics Perspective," *Granular Matter*, vol. 9, no. 1-2, pp. 109-134, 2006.
- [31] J. Hartung, G. Knapp, and B. K. Sinha, *Statistical meta-analysis with applications*, vol. 738 ed. Wiley.com, 2011.
- [32] C. Duriez, "Control of elastic soft robots based on real-time finite element method," in *IEEE International Conference on Robotics and Automation*, 2013, pp. 3982-3987.
- [33] A. A. Stanley, D. Mayhew, R. Irwin, and A. M. Okamura, "Integration of a particle jamming tactile display with a cable-driven parallel robot," in *Eurohaptics Conference*, 2014, p. Accepted.



**Andrew A. Stanley** (S'10) received the BSE degree in mechanical engineering and applied mechanics from the University of Pennsylvania in 2011 and the MS degree in mechanical engineering from Stanford University in 2013. He is currently working toward the PhD degree at Stanford University, supported by a US National Science Foundation Graduate Research Fellowship. He is a student member of the IEEE.



**Allison M. Okamura** (S'98-A'00-M'03-SM'09-F'11) received the BS degree from the University of California at Berkeley in 1994, and the MS and PhD degrees from Stanford University in 1996 and 2000, respectively, all in mechanical engineering. She is currently Associate Professor in the mechanical engineering department at Stanford University. She was previously Professor and Vice Chair of mechanical engineering at Johns Hopkins University.

She has been an associate editor of the IEEE Transactions on Haptics, an editor of the IEEE International Conference on Robotics and Automation Conference Editorial Board, and co-chair of the IEEE Haptics Symposium. Her awards include the 2009 IEEE Technical Committee on Haptics Early Career Award, the 2005 IEEE Robotics and Automation Society Early Academic Career Award, and the 2004 NSF CAREER Award. She is an IEEE Fellow.